Available online at www.sciencedirect.com
SCIENCE DIRECT®
Journal of Solid State Chemistry 177 (2004) 4516–4527
JOURNAL OF SOLID STATE CHEMISTRY
www.elsevier.com/locate/jssc

Insights on the origin of the structural phase transition in $BaV_{10}O_{15}$ from electronic structure calculations and the effect of Ti-doping on its structure and electrical transport properties

C.A. Bridges[a,1], J.E. Greedan[a,*], Holger Kleinke[b]

[a] *Department of Chemistry and Brockhouse Institute for Materials Research, McMaster University, 1280 Main Street W. (ABB-424), Hamilton, Ontario, Canada L8S 4M1*

[b] *Department of Chemistry, University of Waterloo, Waterloo, Ontario, Canada*

Received 2 July 2004; received in revised form 23 August 2004; accepted 30 August 2004
Available online 11 November 2004

Abstract

Band structure calculations at the level of LMTO-ASA provide insight into the electronic structure of $BaV_{10}O_{15}$ and the origin of the structural phase transition. A crystal orbital Hamiltonian population/integrated crystal orbital Hamiltonian population analysis provides evidence that the crystallographic phase transition is driven by V–V bond formation. As well, the energy bands near the Fermi level are very narrow, <1 eV, consistent with the fact that the observed insulating behavior can be due to electron localization via either Mott-Hubbard correlation and/or Anderson disorder. The partial solid solution, $BaV_{10-x}Ti_xO_{15}$, was examined to study the effect of Ti-doping at the V sites on the structure and electronic transport properties. In spite of the non-existence of "$BaTi_{10}O_{15}$", the limiting $x = 8$, as indicated by a monotonic increase in the cell volume and systematic changes in properties. This limit may be due to the difficulty of stabilizing Ti^{2+} in this structure. For $x = 0.5$ both the first order structural phase transition and the magnetic transition at 40 K are quenched. The samples obey the Curie–Weiss law to $x = 3$ with nearly spin only effective moments along with θ values which range from -1090 K ($x = 0.5$) to -1629 K ($x = 3$). For $x > 3$ a very large, $\sim 2 \times 10^{-3}$ emu/mol, temperature independent (TIP) contribution dominates. Conductivity measurements on sintered, polycrystalline samples show semiconducting behavior for all compositions. Activation energies for Mott hopping derived from high temperature data range from ~ 0.1 eV for $x = 0-1$ and fall to a plateau of 0.06 eV for $x = 3-7$. Low temperature data for $x = 3$, 5 and 7 show evidence for Mott variable range hoping (VRH) with a $T^{1/4}$ law and in one case between 5 and 17 K, a Efros-Shklovskii correlated hopping, $T^{1/2}$ law, was seen, in sharp contrast to $BaV_{10}O_{15}$ where only the E-S law was observed up to 75 K. Seebeck coefficients are small ($<35\,\mu V/K$), positive, roughly TIP and increase with increasing x up to $x = 5$. This may point to a Heikes hopping of holes but a simple single carrier model is impossible. The compositions for $x > 3$ are remarkable in that local moment behavior is lost, yet a metallic state is not reached. The failure of this system to be driven metallic even at such high doping levels is not fully understood but it seems clear that disorder induced carrier localization plays a major role.

Keywords: Band structure calculations: LMTO, COHP and ICOHP; Single crystal X-ray diffraction; Neutron powder diffraction; Electrical conductivity; Variable range hopping; Magnetic susceptibility; Seebeck coefficients

1. Introduction

In a recent report the unusual mixed valence vanadium oxide, $BaV_{10}O_{15}$, formally containing the rare V^{2+} oxidation state, was investigated extensively with regard to crystal structure and thermal and

*Corresponding author. Fax: +1-905-521-2773.
E-mail address: greedan@mcmaster.ca (J.E. Greedan).
[1] Currently at the Department of Chemistry, University of Liverpool, Liverpool, UK.

0022-4596/$ - see front matter © 2004 Elsevier Inc. All rights reserved.
doi:10.1016/j.jssc.2004.08.044

electrical transport properties [1]. This material exhibits a first order crystallographic phase transition below a characteristic temperature, T_s, within the range 105–135 K, depending on the degree of sample oxidation, driven apparently by partial V–V bond formation. There is no convincing crystallographic evidence for charge ordering of the V^{2+} and V^{3+} ions on the vanadium sublattice. The transport properties reflect the phase transition, showing a marked, but not discontinuous decrease in conductivity below T_s. The material remains semiconducting over the entire temperature range studied with an activation energy ~0.1 eV above T_s and evidence exists for variable range hopping (VRH) of the correlated Efros-Shklovskii (ES) type over a surprisingly wide temperature range, 35–70 K. The thermopower is very small, $\sim +1\,\mu V/K$ at room temperature and increases markedly to near $+200\,\mu V/K$ below T_s. The thermopower data are inconsistent with a simple one carrier hopping model (assuming that the V^{2+} ions supply the carriers) both in sign and magnitude and seem to demand a two carrier picture with nearly equal contributions from n- and p-type carriers at room temperature, above T_s, and with the selective removal of n-type carriers below due to the bond formation.

Insight into the electronic structure of the $x = 0$ phase and the origin of the structural phase transition can be provided by detailed calculations, for example at the LMTO-ASA level [2]. This is true in spite of the fact that band structure methodologies generally ignore the factors which result in an insulating ground state for transition metal oxides, such as strong electron correlation (Mott-Hubbard localization) and disorder (Anderson localization). It is of interest to study the effects of chemical substitutions at the vanadium sites, in particular to determine if the system can be driven into a metallic state. As the corresponding Cr analogs, $BaCr_{10}O_{15}$ and $SrCr_{10}O_{15}$, are insulating, the effects of Ti doping are examined here [3]. Results for Ti doping of structurally related vanadium oxides are encouraging. For example just 5.5% Ti doping of the Mott insulator, V_2O_3, suppresses the metal to insulator transition (MIT) at 160 K and stabilizes the metallic ground state at all temperatures [4]. Ti_2O_3 is of course nearly metallic and other materials in the Ba–Ti–O system, such as $Ba_2Ti_{13}O_{22}$, which contains nearly all Ti^{3+} and has a crystal structure similar to that of $BaV_{10}O_{15}$, are reported to be metallic [5,6]. Nonetheless, an isostructural "$BaTi_{10}O_{15}$" phase has not been reported, so it will be of interest to establish the limits of Ti solubility in this structure type. Limited solid solubility of Ti in related vanadates such as $Sr(V_{6-x}Ti_x)O_{11}$ has been reported, $x \sim 1.5$ at 1200 °C, where the corresponding titanate phase does not exist [7].

2. Computational and experimental procedures

2.1. Electronic structure calculations

We utilized the LMTO method (LMTO = linear muffin tin orbitals), with the atomic spheres approximation (ASA) for the electronic structure calculations on both modifications of $BaV_{10}O_{15}$ [2,8]. In the LMTO approach, the density functional theory is used within the local density approximation (LDA) [9]. The integrations in k space were performed by an improved tetrahedron method [10] on grids of 64 independent k points of the first Brillouin zone in the case of the low temperature modification (high temperature form: 129 k points).

2.2. Sample preparation

Samples of $Ba(V_{10-x}Ti_x)O_{15}$ were prepared using the same approach as for $BaV_{10}O_{15}$ described previously [1]. Appropriate amounts of $Ba_3V_2O_8$, V metal, V_2O_3 and Ti_2O_3 were ground and mixed thoroughly in an agate mortar and pestle. Pellets were pressed and loaded into a molybdenum crucible which was sealed by welding under purified argon.

The crucible and contents were heated in an induction furnace at temperatures between 1500 and 1600 °C as monitored using an optical pyrometer. The crucibles were heated to the reaction temperature over 7 h, maintained for 17 h and then quenched by turning off the r.f. generator. $Ba_3V_2O_8$ was prepared by heating $BaCO_3$ and V_2O_5 in air at 950 °C for 24 h and V_2O_3 was obtained by H_2 reduction of V_2O_5 at 700 °C for 24 h. The oxygen stoichiometry of V_2O_3, V metal and Ti_2O_3 were monitored using thermogravimetric analysis (TGA) and the reaction amounts were adjusted accordingly.

In a few cases, crystal growth was attempted using a Tri-Arc furnace under an atmosphere of purified argon. A ~3 g boule of the starting material was melted on a water-cooled copper hearth and a water-cooled tungsten rod was lowered into contact with the molten boule and then withdrawn at a rate of 45 mm/h. The resulting rod contained regions of single crystals of dimension ~1 mm.

2.3. X-ray powder diffraction

X-ray powder diffraction data were obtained using either a Guinier-Hägg camera with a silicon internal standard and Cu$K\alpha_1$ radiation or a Bruker D8 Advance diffractometer with Cu$K\alpha$ radiation. Unit cell constants were refined from ~30 indexed reflections (Guinier data) using standard least squares software and by Rietveld refinement of the D8 data.

2.4. Neutron powder diffraction

Data were collected on the C2 diffractometer operated by the Neutron Program for Materials Research of the National Research Council of Canada at the Chalk River Laboratories of AECL Ltd. A neutron wavelength of 1.3282 Å was used. The sample was contained in a helium-filled vanadium can which was sealed with and an indium gasket. Data were taken both at ambient temperature and 30 K using a closed-cycle refrigerator.

2.5. X-ray single crystal diffraction

Single crystals of nominal composition, BaV_9TiO_{15} ($x = 1$), grown in the Tri-Arc furnace as described above, were ground into spheres. Data were collected using Mo radiation from a Siemens rotating anode, a Bruker/Siemens P4 diffractometer and a SMART CCD area detector. Data processing and analysis were performed using the SHELXTL software package [11]. Absorption corrections were carried out using SADABS [12], including a $\lambda/2$ correction.

2.6. D.C. magnetic susceptibility measurements

Magnetic susceptibility data were collected using a Quantum Design MPMS system from 2 to 600 K. The region between 300 and 600 K was attained with the use of an oven insert.

2.7. Electrical transport measurements

Resistivity data were collected on an Oxford Instruments MagLab system using a standard four probe geometry as described in [1].

2.8. Thermoelectric power

Measurements of the thermoelectric power were obtained using a home-built apparatus which has been described previously [13].

2.9. Thermogravimetric analysis

Oxidative weight gain experiments were carried out using a Netzsch STA409 system in air.

3. Results and discussion

3.1. Electronic structure calculations

Results of LMTO-ASA calculations carried out on the $x = 0$ end member can provide insights into some of the properties observed. Recall that this material undergoes a structural phase transition which has been attributed to V–V bond formation between a subset of atoms in the vanadium sublattice [1]. To facilitate the discussion which follows, we present a figure from [1] which shows the V sites in one layer for both the high and low temperature forms (HT/LT), (Fig. 1). Comparison of the full DOS for the high and low temperature structures (HT/LT), Fig. 2 (top), provides no obvious clues to the origin of the phase transition. However, crystal orbital Hamiltonian population (COHP) plots [14] emphasizing the contribution of selected V–V bonds, namely V2–V3 at 2.73 and 2.99 Å in the HT form and the corresponding V2B–V3 at 2.53 and 3.09 Å the LT form, Fig. 2 (bottom), show filled, strong bonding states below E_F and corresponding, empty antibonding states above E_F for the bond at 2.53 Å. An Integrated COHP (ICOHP) bond length/bond strength analysis has also been carried out [15]. This approach has proved valuable in understanding the origin of structural distortions, for example, recently in Ti_2Sb [16]. Such an analysis is shown in Fig. 3, quantifying the

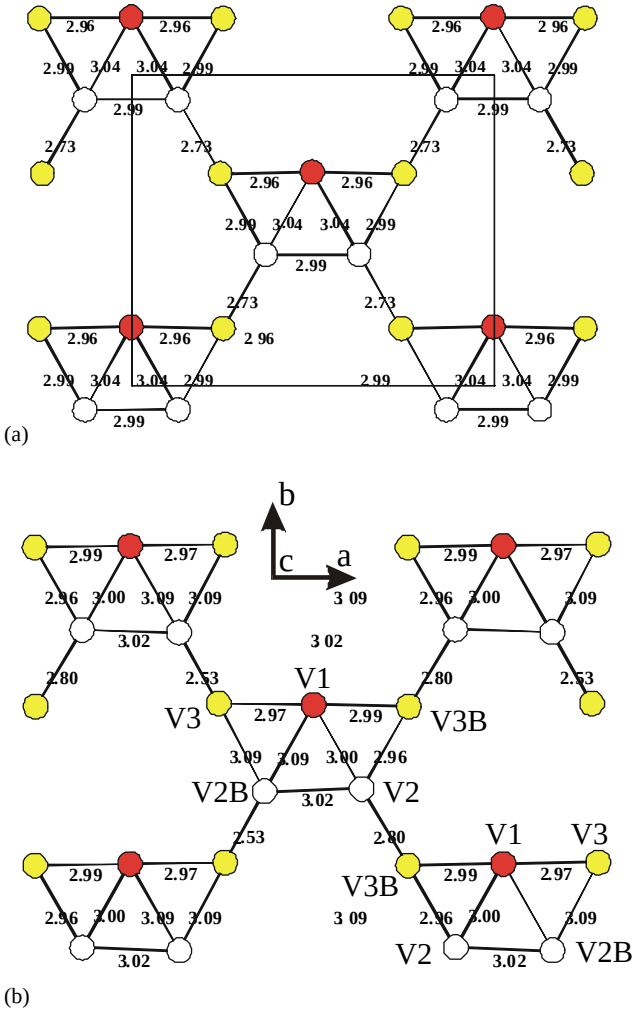

Fig. 1. Changes in V–V distances for $BaV_{10}O_{15}$ within one V-layer as a result of the *Cmca* (HT) to (LT) *Pbca* phase transition.

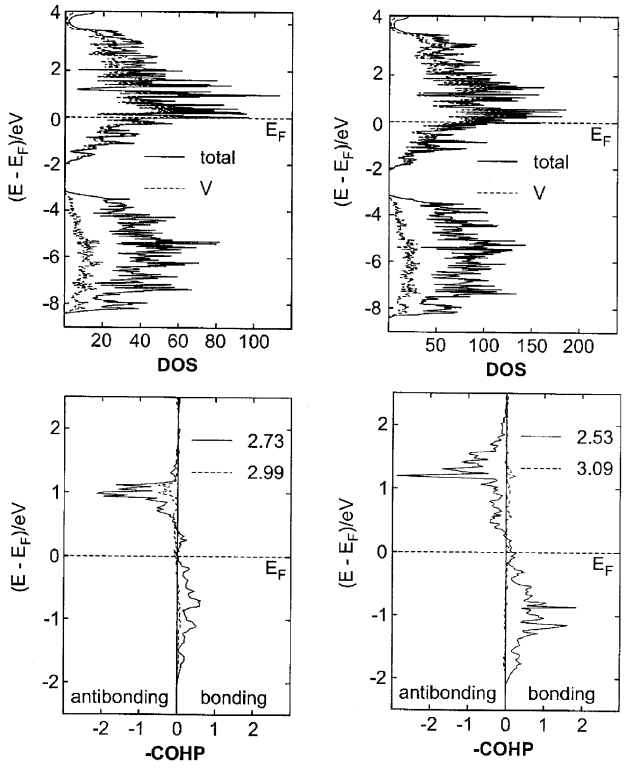

Fig. 2. (Top) Density of States for $BaV_{10}O_{15}$, high temperature phase *Cmca* (left) low temperature phase *Pbca* (right). (Bottom) COHP Curves for V2–V3 bonds in the high temperature form (left) and the V2B–V3 bonds in the low temperature form (right).

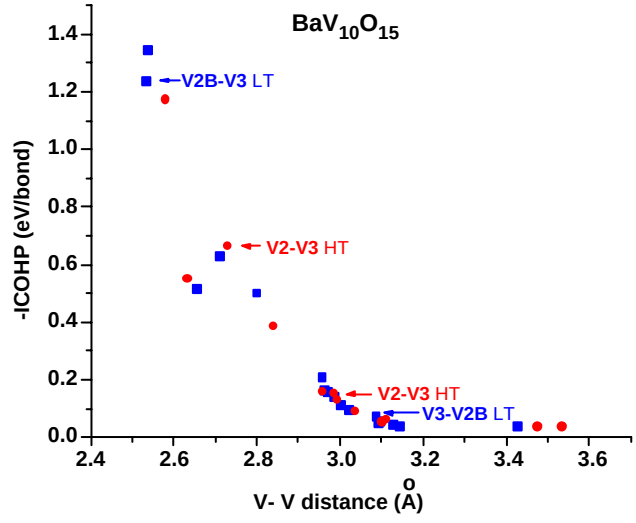

Fig. 3. ICOHP plots versus bond length for selected V2–V3 and V2B–V3 bonds in the high (squares) and low (circles) temperature forms.

net stabilization which accompanies the bond length changes involved in the HT/LT phase transition. For example, the V2–V3 bonds in the HT phase at 2.73 and 2.99 Å have ICOHP values of −0.6 and −0.1 eV/bond, respectively. These transform into V2B–V3 bonds in the LT phase at 2.53 and 3.09 Å, with ICOHP values of

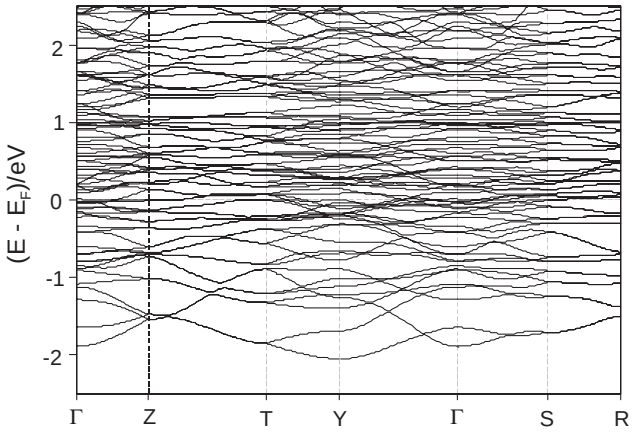

Fig. 4. Portion of the band structure of the high temperature form of $BaV_{10}O_{15}$ showing the presence of very narrow bands near the Fermi level.

−1.3 and −0.05 eV/bond, respectively [1]. The net stabilization accompanying these changes is ∼−0.7 eV.

Additionally, from Fig. 4, which shows the detailed band structure within the mainly V-d band, the electronic states near the Fermi level are predominantly very narrow, <1 eV in width. This suggests that either Mott-Hubbard correlation and/or Anderson localization effects could easily induce the insulating behavior observed. Note also that Ti-doping will push the Fermi level toward the bottom of the band where the average individual band widths are greater suggesting the possibility of inducing metallic behavior. However, it is near the bottom of the band where localized states influenced by the mobility edge will be found. Thus, there will be a competition between the band width and disorder induced localization associated with the Ti-doping experiments. This general situation has been discussed in detail by Mott, for example [17].

A final remark should be made before leaving the computational results. Those reported here were obtained using the LDA (local density approximation) rather than the LSDA (local spin density approximation). At first glance it would seem, given the magnetic evidence for local moment behavior at the V sites and the strong antiferromagnetic correlations, that the latter approximation would be more appropriate. In fact the ICOHP results were not significantly different between the two levels of approximation. Moreover, since the structural transition occurs below 135 K and the magnetic transition is at 40 K, where spin polarization might play a more important role, the LDA approach is better suited to gain insight into the driving force for the structural phase transition.

3.2. *Extent of solid solution in* $Ba(V_{10-x}Ti_x)O_{15}$

Several attempts to prepare the all titanium, $x = 10$, phase were unsuccessful. Nonetheless, perhaps surpris-

ingly, the solid solution appears to extend up to $x = 8$ or 80% on an atomic basis. Samples up to $x = 6$ could be prepared in essentially single phase form, while for $x = 7$ and 8, low levels of impurity phases were observed but a clear evolution of lattice constants was observed. This is a much higher extent of solubility than reported for the related series, $Sr(V_{6-x}Ti_x)O_{11}$ as mentioned earlier, where $x = 1.5$ at most or 25% substitution on an atomic basis. Apart from the difference in crystal structure, the preparations reported here were carried out at much higher temperatures, 1500 to 1600 °C, than the 1200 °C used for $Sr(V_{6-x}Ti_x)O_{11}$. The evolution of the unit cell constants is displayed in Figs. 5a–d.

The cell constants and cell volume increase systematically with Ti substitution as expected given that Ti^{3+} is slightly larger than V^{3+} (0.67 Å for the former and 0.64 Å for the latter) [18]. A linear increase is seen to $x = 8$ for **b,c** and the cell volume but the increase in **a** is non-linear. The unit cell is the same orthorhombic cell, *Cmca*, as found for $BaV_{10}O_{15}$ at room temperature for all phases studied. A likely reason for the non-existence of $BaTi_{10}O_{15}$ is the difficulty of stabilizing the +2 oxidation state of titanium in an oxide lattice. Apart from the highly non-stoichiometric $TiO_{1\pm x}$ there are few credible reports of complex oxides containing Ti^{2+}. It is worth noting that the limiting Ti composition, $x = 8$, could imply the valence combination $BaTi_8^{3+}V_2^{2+}O_{15}$ and further substitution beyond $x = 8$ would require the formation of some Ti^{2+}.

3.3. TGA weight gain analysis

Four samples, $x = 1$, 3, 5 and 7, which were used subsequently for the electrical transport, magnetic susceptibility and thermopower measurements were analyzed by heating in air and observing the weight gain. From the results in Table 1, samples for $x = 1$, 3 and 5 were slightly oxidized and $x = 7$ was slightly reduced relative to the ideal stoichiometry.

In Table 1, the composition of the oxidized phases has been expressed for convenience as an oxygen excess. This is unlikely as the O-sublattice is close packed and a

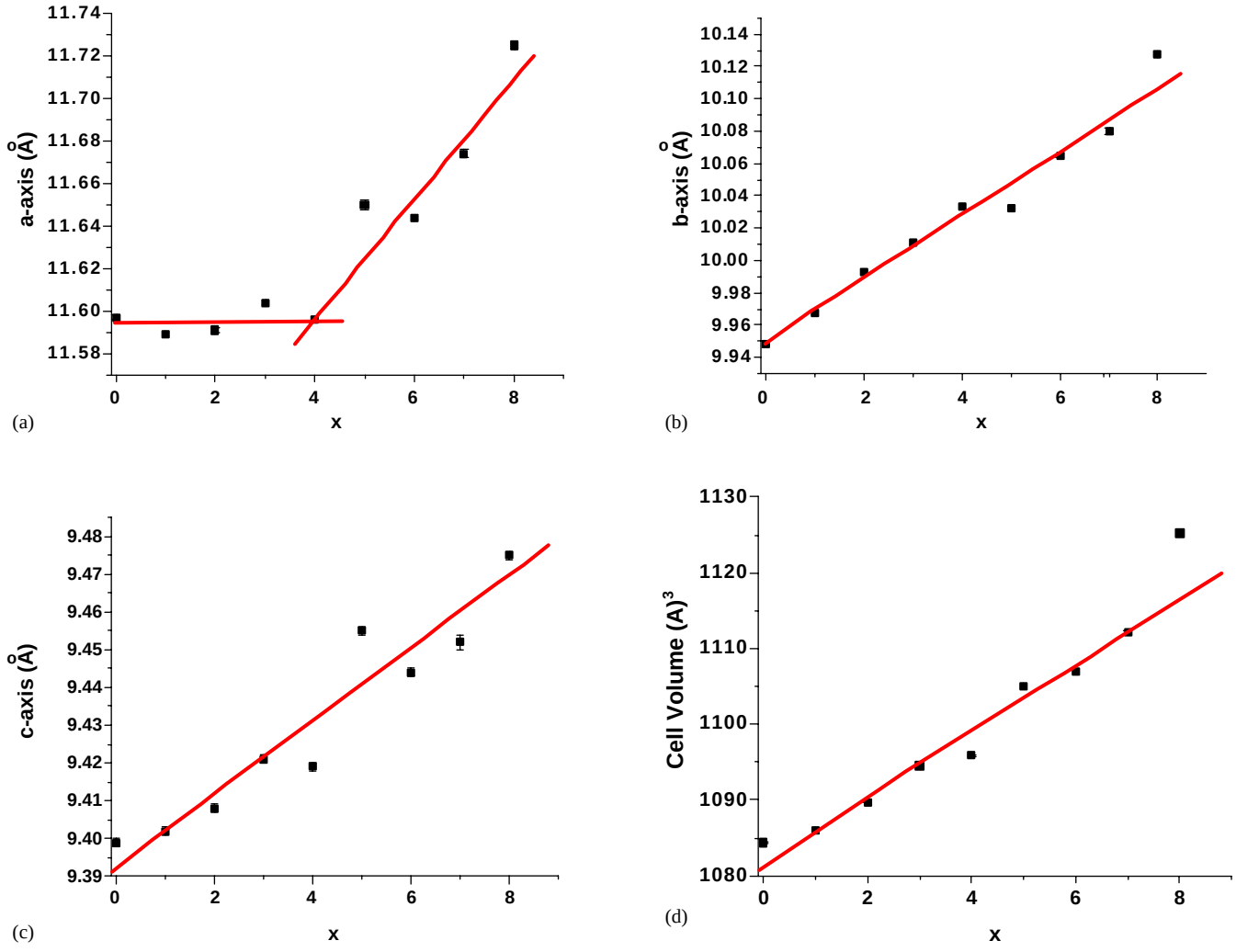

Fig. 5. (a–d) Evolution of the unit cell constants and the cell volume in $BaV_{10-x}Ti_xO_{15}$ from Guinier X-ray data.

Table 1
Weight gain analysis by TGA for $BaV_{10-x}Ti_xO_{15+y}$

x	Weight gain (%)	y
1	18.65	+0.17
3	16.58	+0.35
5	14.36	+0.59
7	14.21	−0.33

cation deficiency, probably on the Ba site, is more probable as was found from ion coupled plasma mass spectrometry (ICPMS) analysis for various samples of "$BaV_{10}O_{15}$" reported in [1]. Unfortunately, it was not possible to carry out ICPMS analysis on the Ti-containing samples due to incomplete dissolution, some residual solid was always in evidence. An attempt to address the issue of Ba deficiency has been made below in the analysis of the single crystal X-ray data for BaV_9TiO_{15}.

3.4. Crystal structure of BaV_9TiO_{15} by single crystal X-ray diffraction

The results of the structure determination at 298 K are displayed in Tables 2a–d. The same space group, *Cmca*, as for the $x = 0$ phase was found. The refinement proceeded smoothly to the atomic and isotropic displacement parameters of Table 2b. Selected metal–oxygen and metal–metal distances are shown in Table 2c. These are also compared with the mean values for the corresponding distances in $BaV_{10}O_{15}$. Note the systematic increases in all mean distances for the Ti substituted sample, consistent with the larger effective size of Ti^{3+} relative to V^{3+} as mentioned above. It was not possible to refine the Ti/V ratio in the sample due to the similarity in scattering power of the two elements so the Ti/V ratio was fixed at 1:9 for the final refinement. Refinement of the fractional occupancy of all sites yielded an overall stoichiometry in agreement with the nominal BaV_9TiO_{15} to within error, thus, the speculation about Ba deficiency is not confirmed by the single crystal X-ray data. A bond valence analysis is shown in Table 2d [19]. The results for the V/Ti sites, denoted S in these tables are consistent with the assumed valences (Ti^{3+}, V^{3+} and V^{2+} randomly distributed over all three sites).

Further details of the crystal structure experiment can be obtained from the Fachinformationzentrum Karlsruhe, 76344 Eggenstein-Leopoldhafen, Germany (fax: (49) 7247-808-666; e-mail: crysdata@fiz-karlsruhe.de) on quoting the depository numbers (CSD) 414183.

3.5. Crystal structure at 30 K

One of the striking features of the parent material, $BaV_{10}O_{15}$, is the first order structural phase transition below 135 K. This is manifested very clearly in the magnetic susceptibility [1]. As will be shown in the following section, the phase transition appears to be quenched for a Ti doping level as low as $x = 0.5$. To investigate a possible structure change neutron diffraction data were collected at 30 and 298 K on the $x = 1.0$ sample as seen in Fig. 6. Apart from very small changes due to shifts in the unit cell parameters with temperature, there is no discernable difference between the two data sets. This verifies the quenching of the crystallographic phase transition by very small Ti doping levels.

3.6. D.C. magnetic susceptiblity

Figs. 7a and 7b show the evolution of the bulk d.c. susceptibility for all compositions studied over the full temperature range, 2–600 K. It is immediately clear that both transitions seen in the $x = 0$ phase, at 135 K (structural) and 40 K (magnetic) vanish even for $x = 0.5$, confirming the neutron diffraction results. Looking more closely, two categories of behavior are clearly seen. From $x = 0$ to 3 the Curie–Weiss law holds (Fig. 7a). The derived Curie–Weiss parameters are listed in Table 3. The Curie constants are consistent with spin-only values calculated assuming the appropriate combinations of $V^{2+}/V^{3+}/Ti^{3+}$ for each composition and the agreement is excellent indicating a local moment picture for the *d*-electrons. Note also the remarkably large, negative Weiss temperatures which range to −1629 K for $x = 3$. A FC/ZFC divergence occurs at low temperatures for each sample between 10 and 15 K, listed in Table 3 as T_D. Thus, the so-called frustration indices, $|\theta_c|/T_D$, are very large as found for the $x = 0$ phase, up to ~136 for $x = 3$, consistent with the geometrical frustration of the V sublattice [1,20]. A more extensive discussion of the magnetic properties of the $x = 0$ to 3 phases, including neutron diffraction, a.c. susceptibility and specific heat data will be presented in a subsequent report.

Beyond $x = 3$, Fig. 7b, the Curie–Weiss behavior, at least up to 600 K, is lost. The FC/ZFC divergence still persists but is found at lower temperatures, ~8 K for $x = 4$ and 5 K for $x = 5$, but is absent, at least to 4 K, for $x = 6$ and 7. The high temperature susceptibility, $T > 300$ K, is essentially temperature independent (TIP) for $x = 5-7$, with very high values, $\chi_{TIP} = 2–3 \times 10^{-3}$ emu/mol. For comparison, for the metallic phase of V_2O_3 just above the MIT, $\chi = \sim 1.5 \times 10^{-3}$ emu/mol [21].

Thus, the susceptibility data are highly informative and allow the following conclusions: (1) Both the crystallographic (135 K) and long-range magnetic (40 K) phase transitions are quenched by small levels of Ti-doping. (2) Local moment behavior persists for Ti doping levels up to 30% but appears to be lost for higher doping levels. This suggests the possibility of a

Table 2
(a) Details of the single crystal X-ray diffraction experiment at 298 K for BaV_9TiO_{15}.

Space group	*Cmca*	Refinement	
A (Å)	11.6322(1) [11.584(4)]	*R*1 ($I>2\sigma$)	0.0251
b (Å)	10.0022(1) [9.946(3)]	*wR*2 ($I>2\sigma$)	0.0573
c (Å)	9.4380(1) [9.383(4)]	*R*1 (all)	0.0284
V (Å^3)	1098.09(2) [1081.1(7)]	*wR*2 (all)	0.0584
Temp. (K)	298	G.O.F.	1.244
Radiation	Mo*K*α		1598
Color	Black	No. reflections	68
Index ranges	$-20\leqslant h\leqslant 16$	No. parameters	0.0073(2)
	$-17\leqslant k\leqslant 17$	Extinction	0.000
	$-16\leqslant l\leqslant 16$	Mean shift/su	

(b) Final atomic and isotropic displacement parameters for BaV_9TiO_{15} at 298 K in *Cmca*

Site	*x*	*y*	*z*	Occupation	U_e (Å^2)
Ba	0	0.5	0	1.0	0.01077(6)
S1	0.5	0.67806(4)	0.13878(4)	V(0.9)Ti(0.1)	0.00676(8)
S2	0.37064(3)	0.41004(3)	0.13878(4)	V(0.9)Ti(0.1)	0.00850(7)
S3	−0.24589(3)	0.67127(3)	0.11059(3)	V(0.9)Ti(0.1)	0.00741(7)
O1	−0.25372(18)	0.5	0	1.0	0.0090(3)
O2	0.11882(12)	0.24686(13)	0.00164(14)	1.0	0.0088(2)
O3	0.25	0.32570(18)	0.25	1.0	0.0075(3)
O4	0.62904(11)	0.58849(13)	0.24374(13)	1.0	0.0073(2)
O5	0.5	0.34238(19)	0.2498(2	1.0	0.0079(3)
O6	0.5	0.5	0	1.0	0.0073(4)

(c) Selected bond distances for BaV_9TiO_{15} in *Cmca* at 298 K (Å).

Bond	Bond length	Bond	Bond length	Bond	Bond length
Ba–O5 (× 2)	2.839(2)	S1–O5	1.951(2)	S3–S3	2.6167(6)
Ba–O2 (× 4)	2.885(1)	S1–O4 (× 2)	2.009(1)	S3–S3	2.6332(6)
Ba–O1 (× 2)	2.951(2)	S1–O2 (× 2)	2.015(1)	S2–S3	2.7560(4)
Ba–O4 (× 4)	2.981(1)	S1–O6	2.2107(4)	S2–S3	2.8558(4)
Mean	2.920 [2.916]	Mean	2.035 [2.034]	S1–S3	2.9686(3)
				S2–S3	2.9980(4)
S2–O3	1.9626(8)	S3–O2	1.994(1)	S2–S2	3.0094(7)
S2–O5	1.972(1)	S3–O1	2.0081(3)	S1–S2	3.0744(5)
S2–O2	2.037(1)	S3–O2	2.026(1)	S1–S2	3.1201(5)
S2–O4	2.057(1)	S3–O3	2.030(1)		
S2–O1	2.071(1)	S3–O4	2.093(1)		
S2–O6	2.1693(3)	S3–O4	2.103(1)		
Mean	2.045 [2.027]	Mean	2.042 [2.026]		

(d) Selected bond valence sums for BaV_9TiO_{15} at 298 K (in v.u.)

Atom	Bond valence[a]	Atom	Bond valence
Ba	2.179	O1	1.950
S1	2.763	O2	2.086
S2	2.675	O3	2.010
S3	2.666	O4	1.819
		O5	1.857
		O6	1.814
	Mean bond valence		
	S = 2.701		
	O = 1.923		

Note: Quantities in square brackets are corresponding values for $BaV_{10}O_{15}$ [3].
[a]The bond valences listed are weighted averages assuming a random distribution of V^{2+}, V^{3+} and Ti^{3+} on the S1–S3 sites [19].

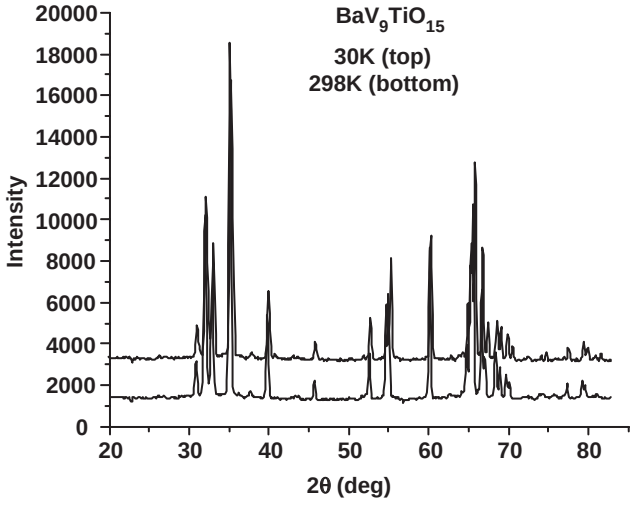

Fig. 6. Comparison of the neutron powder diffraction data for BaV_9TiO_{15} at 298 and 30 K showing no apparent change in crystal structure.

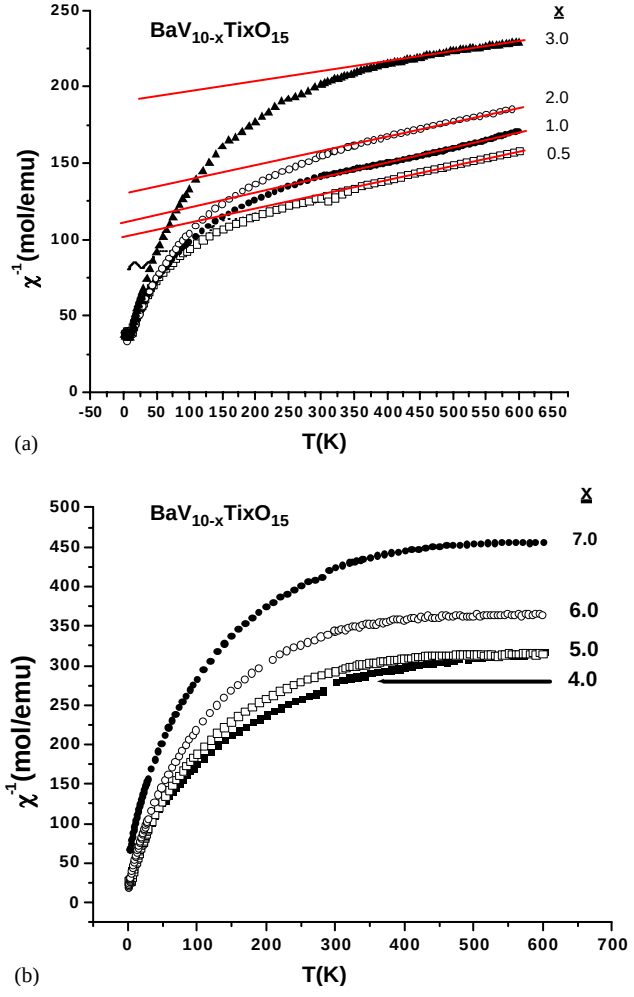

Fig. 7. (a) d.c. Magnetic susceptibility for $BaV_{10-x}Ti_xO_{15}$ for $x = 0.5-3$. Note that the Curie–Weiss law holds up to 600 K, and (b) for $x \geqslant 4$ a large TIP term dominates for $T > 300$ K.

fundamental change in the state of the *d*-electrons for $x > 3.0$.

3.7. Electrical transport, d.c. conductivity

Results for five compositions, $x = 0$, 1, 3, 5 and 7 are compared in Fig. 8 over the range 5 K (in some cases) to 300 K. For the more resistive samples the minimum temperature is higher due to experimental limitations but for $x = 5$ and 7, the data extend to 5 K. Data for two samples of $x = 0$ are included, $T_s = 105$ and 135 K, which span the range of behavior for the un-doped material. It is clear that the conductivity is enhanced by several orders of magnitude for the Ti-doped samples relative to the $x = 0$, $T_s = 135$ K sample, especially at lower temperatures. The differences are much smaller near room temperature with just slightly more than a factor of 10 separating the samples. As well, it is clear that none of the compositions show metallic behavior within the examined temperature range. At relatively high temperatures, all samples appear to follow an Arrhenius law (Fig. 9 (left)). The data can be fitted, equally well, using the adiabatic Mott polaronic model, Eq. (1), as discussed in [1],

$$\sigma = AT^{-1}[\exp(-W/kT)], \quad (1)$$

where W is the activation energy for the hopping of a small polaron and the prefactor A is related to a characteristic polaron frequency. No attempt was made to isolate a characteristic frequency from the fitted values of A as it is not clear how to estimate the polaron concentration. As pointed out in [1], even for the $x = 0$ case, the conduction mechanism must involve both electron and hole transport. Questions can be raised regarding the significance of W in a multi-carrier system such as this and it is best to take the value as the average for all of the hopping processes occurring. Nonetheless, the trend in W as the Ti content increases, Fig. 9 (right), is clear. There is a small decrease at $x = 1$ and then a plateau for $x = 3$–7. This is evidence for lower activation energy for hopping involving Ti sites. Indeed, it appears that by $x = 3$ a percolation threshold has been reached such that all hops are through a network including only Ti sites.

3.8. Low temperature conductivity

For materials with such a high level of disorder, it is expected that some form of VRH will be obtained at sufficiently low temperatures [22]. Evidence for VRH is in the form of an expression such as below [22], Eq. (2).

$$\sigma = A \exp(-T_0/T^n). \quad (2)$$

For hopping in three dimensions, the exponent, n, can be either $\frac{1}{4}$ for conventional VRH [22] or $\frac{1}{2}$ if correlation is taken into account [23], the Efros-Shklovskii (ES)

Table 3
Fitting constants derived from a Curie–Weiss analysis of data for $BaV_{10-x}Ti_xO_{15}$, $x = 0$–3

x	C_{obs} (emuK/mol)	$C_{s.o}$ (eumK/mol)[a]	θ_c (K)	T_D (K)	$\lvert\theta_c\rvert/T_D$
0.0	11.6(1)	11.74	−1156(15)	40	29
0.5	10.7(1)	11.44	−1091(14)	13	84
1.0	10.8(1)	11.125	−1322(20)	15	88
2.0	10.6(1)	10.5	−1369(17)	14	98
3.0	9.5(1)	9.375	−1629(30)	12	136

[a]Calculated assuming V^{2+}, V^{3+} and Ti^{3+}.

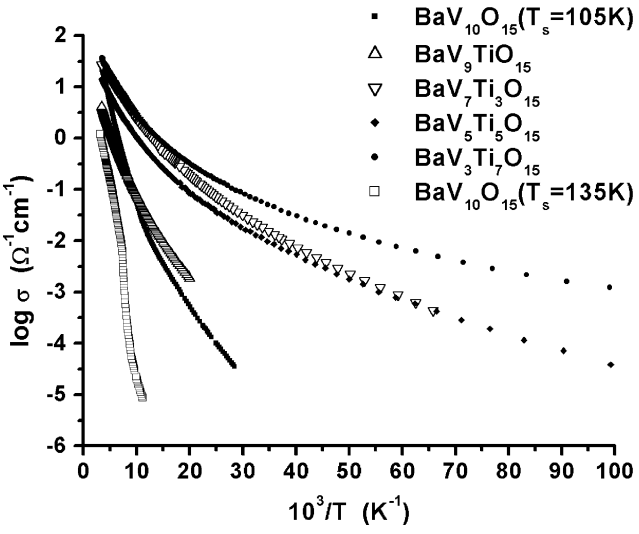

Fig. 8. Temperature dependence of the d.c. conductivity for $BaV_{10-x}Ti_xO_{15}$, $x = 0$, 1, 3, 5.

model. As mentioned in [1], it is often difficult to distinguish between the two power laws with a conventional analysis, so the Hill-Zabrodskii method [24] is often applied. Here an effective activation energy is defined as

$$dE = -1/T\, d(\ln \sigma)/d(1/T) \quad (3)$$

and the exponent, n, in Eq. (2) can be derived from a plot of $\log dE$ vs. $\log T$.

Using such an approach, an exponent of $n = \frac{1}{2}$ was found at low temperatures for $BaV_{10}O_{15}$ ($T_s = 105$ K). A similar analysis was applied to the samples studied here with $x = 3$, 5 and 7. The limited data for $x = 1$ did not include sufficiently low temperatures.

The case for $x = 5$ is shown in Fig. 10a where the data extend to 5 K. Here, both laws can be found with an exponent of $n = \frac{1}{2}$ for the lowest temperatures which gives way to the $n = \frac{1}{4}$ law above ~17 K. The results for $x = 3$, Fig. 10b, are similar but unfortunately the lowest temperature reached is 18 K. The exponent found, $n = 0.31(1)$, is close to $\frac{1}{4}$ and suggests parallel behavior to the $x = 5$ material. $x = 7$, Fig. 10c, presents a radically different situation, wherein an anomalous exponent of $n \sim 0.10(1)$ seems to hold over a very wide range from ~13 to 80 K. The meaning of such an exponent is not clear.

Considering the results for $x = 0$, 3 and 5 a trend appears. The minimum level of site disorder in this series occurs for $x = 0$. Here, the correlated ES VRH law holds over a surprisingly wide temperature range, 35–70 K, which indicates that electron correlation is a determining factor, along with disorder, for the transport behavior at low temperatures. As disorder levels on the metal sites rise with increasing x, the temperature

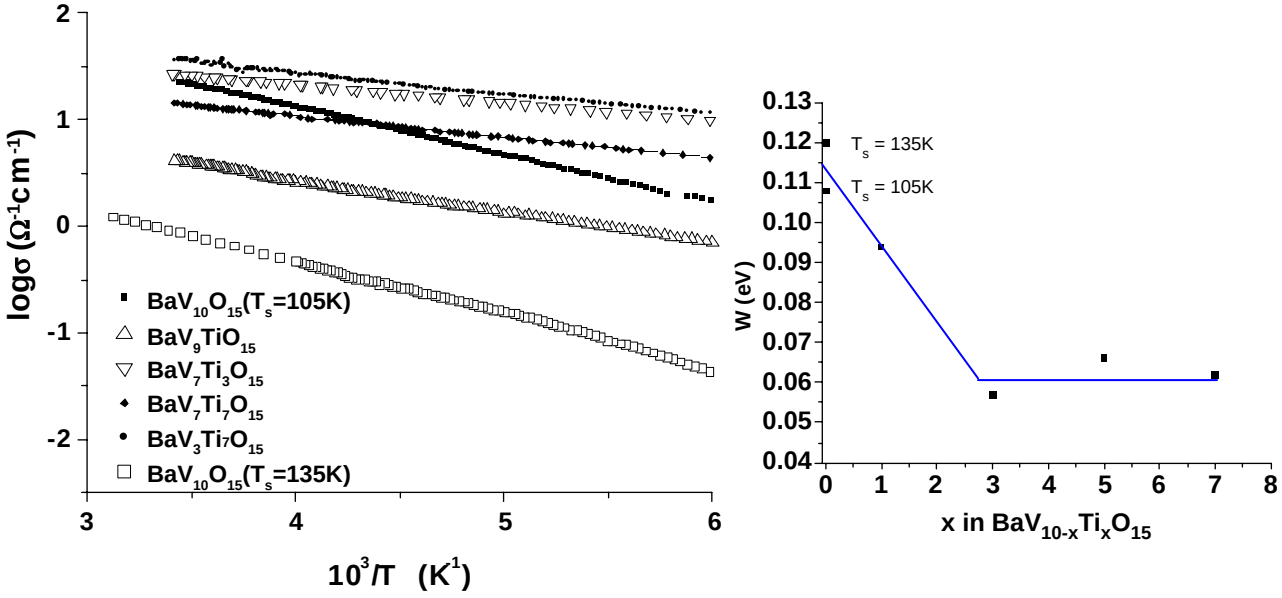

Fig. 9. (Left) Thermally activated conductivity at high temperatures for $BaV_{10-x}Ti_xO_{15}$, $x = 0$, 1, 3, 5 and 7. (Right) Variation of the activation energy for Mott small polaron hopping for $x = 0$, 1, 3, 5 and 7. Note the plateau, $W \sim 0.06$ eV for $x = 3-7$.

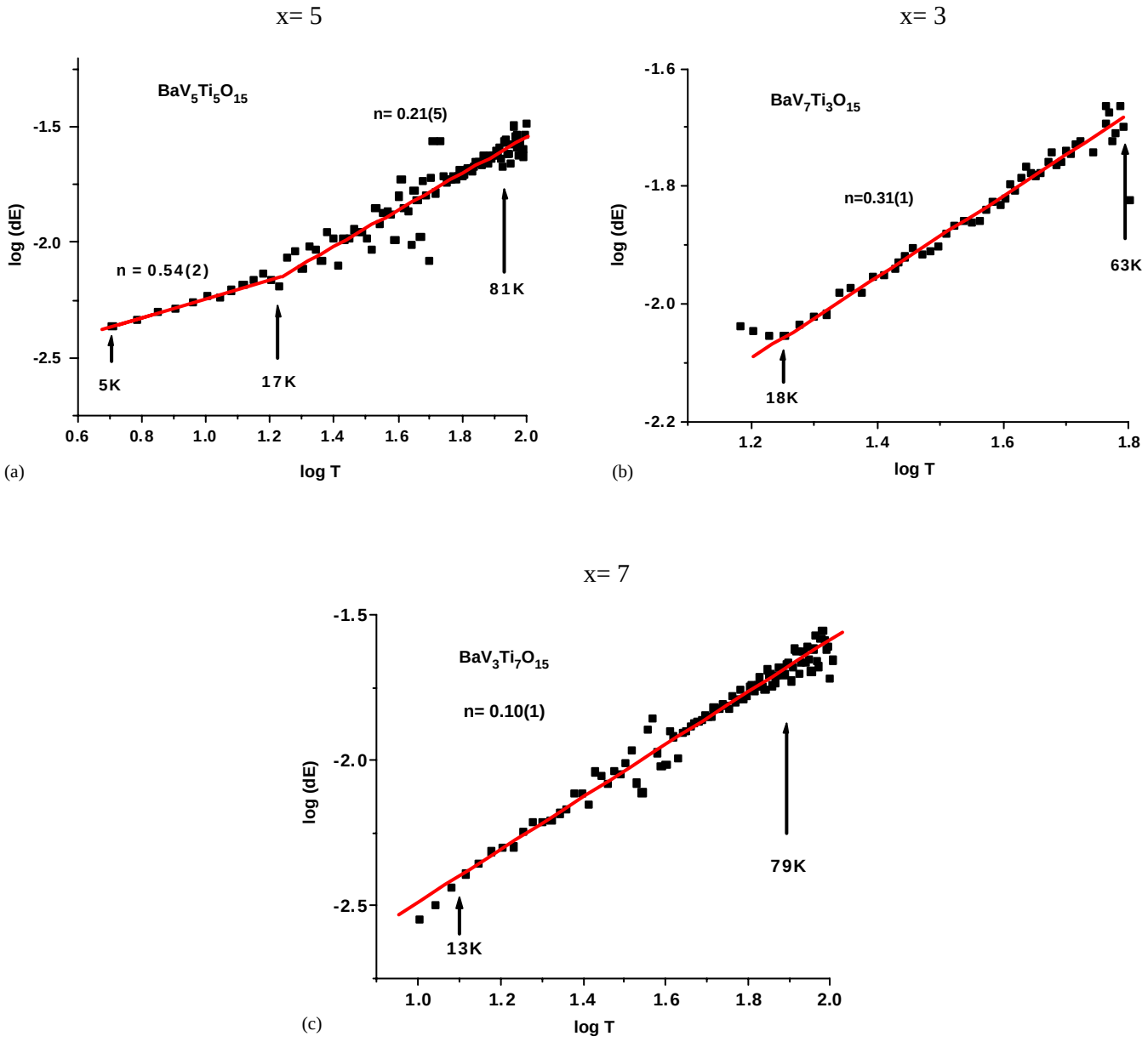

Fig. 10. Hill–Zabrodski analysis of the low temperature conductivity for $BaV_{10-x}Ti_xO_{15}$ showing evidence for VRH. (a) $x = 5$, (b) $x = 3$, and (c) $x = 7$.

range over which ES VRH is observed moves lower, indicating a diminished role for correlation. This is reasonable in that as Ti is substituted for V, the disorder level increases and the average correlation energy decreases. Nonetheless, the highly anomalous exponent found for the maximal level of Ti substitution, $x = 7$, cannot be understood in any simple way.

3.9. Thermopower measurements

Thermopower data can provide evidence complementary to conductivity and susceptibility regarding the state of the *d*-electrons in these materials. Recall that for $x \geqslant 4$ the magnetic susceptibility at high temperatures is TIP, yet the conductivity is still activated, results which are difficult to reconcile. The temperature dependence of the Seebeck coefficient is shown in Fig. 11a for $x = 0$ to 7. Note first, the lack of evidence for a phase transition for $x > 0$, confirming the results from neutron diffraction, susceptibility and conductivity data, Figs. 6–8, respectively, and that the thermopower remains positive and small in value for all $x > 0$. To emphasize the behavior of the $x > 0$ samples Fig. 11b is shown. Apart from the absence of a phase transition, the results are very similar to those for $x = 0$. The data are roughly TIP and small in magnitude, $< 35\,\mu V/K$.

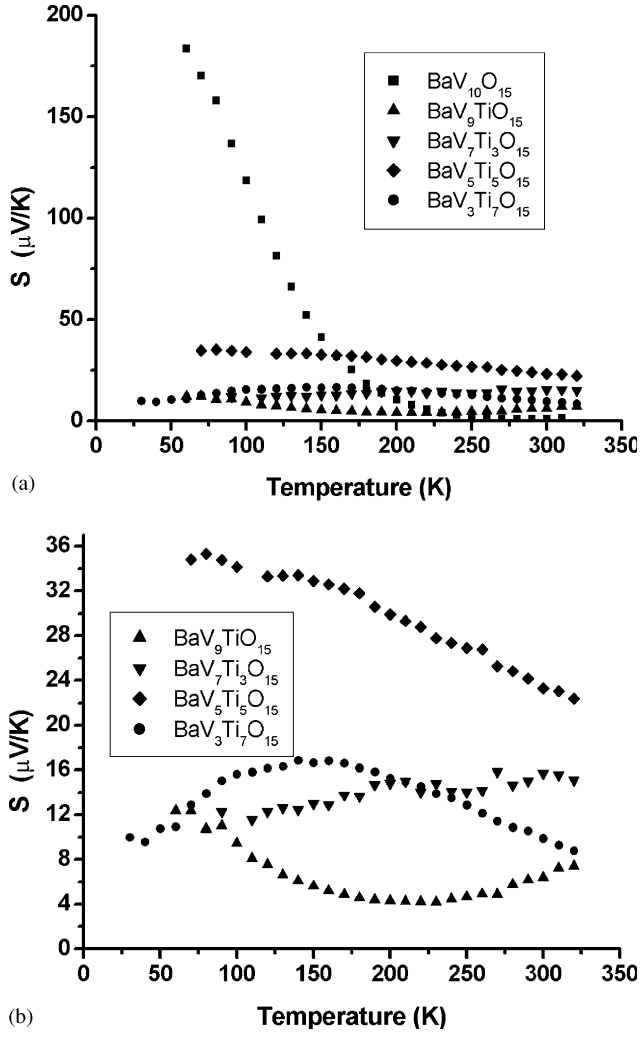

Fig. 11. (a) Comparison of the Seebeck coefficient temperature dependence for $BaV_{10-x}Ti_xO_{15}$ for $x = 0$, 1, 3, 5 and 7. (b) Comparison of data for samples with $x > 0$.

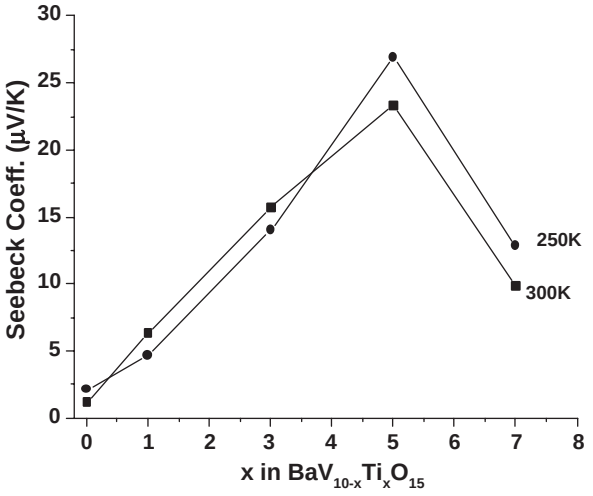

Fig. 12. The linear dependence of the Seebeck coefficient on x up to $x = 5$ at 300 and 250 K.

Taken at face value, with no other information, one could interpret these thermopower data as consistent with metallic behavior for all compositions, based on the small values.

Nonetheless, that would be at odds with the conductivity data, which show an inverse correlation between absolute conductivity and thermopower. That is, the $x = 0$ phase shows simultaneously the smallest conductivity and smallest thermopower. While conceding some ambiguity, a more consistent interpretation assigns the small and roughly TIP thermopower to a two carrier hopping model with the hole contribution dominant, as with the $x = 0$ phase [1]. Note also that the Seebeck coefficient increases linearly with increasing Ti content, as expected from the increased hole concentration (Ti^{3+} having one fewer electron than V^{3+}) up to $x = 5$, Fig. 12. The origin of the decrease for $x = 7$ is not currently understood. The $x = 1$ and 3 phases show nearly TIP behavior. For both the $x = 5$ and 7 phases a weak, linear temperature dependence (with a negative slope) at higher temperatures is seen. Such behavior is not easily interpreted but is not consistent in detail with metallic behavior. For example a p-type metal would show a linear temperature dependence but with a positive slope [25].

4. Summary and conclusions

Computational studies of $BaV_{10}O_{15}$ using the LMTO-ASA method in the LDA approximation in both the high and low temperature forms provide further evidence that the HT/LT structural phase transition in this material is driven by V–V bond formation between atoms which are only a subset of the V-sublattice. Comparison of changes in ICOHP values for bonds, which shorten and lengthen as a result of the transition are especially convincing. The effects of Ti-substitution for V was also studied to determine if the materials can be driven into a metallic state.

The system $BaV_{10-x}Ti_xO_{15}$ shows a surprisingly large range of substitution, up to $x = 8$, given that the $x = 10$, all Ti phase, "$BaTi_{10}O_{15}$", does not exist. As for $x > 8$, the formation of Ti^{2+} would be required, it is inferred that the difficulty in stabilizing this state in oxides is the factor limiting the extent of solid solution. The structural phase transition in the $x = 0$ end member is quenched for substitution levels as low as $x = 0.5$. The electronic effects of Ti doping are somewhat surprising. While even 5% of Ti doping in V_2O_3 is sufficient to stabilize a metallic state and the structurally and electronically similar material, $Ba_3Ti_{13}O_{22}$, is metallic, no level of doping up to the limit of $x = 7$ can drive $BaV_{10-x}Ti_xO_{15}$ metallic. While local moment behavior

in the magnetic susceptibility is lost by $x \sim 4$–5, conductivity and thermopower data on sintered, polycrystalline samples show evidence for Mott polaronic hopping at high temperatures and Mott ($T^{1/4}$ law) VRH at low temperatures. This suggests that disorder induced (Anderson) localization [26] is a major factor in inhibiting the establishment of a metallic state in this system.

Acknowledgments

J.E.G. and H.K. acknowledge support from the Natural Sciences and Engineering Research Council of Canada in the form of a Discovery Grant. H.K. thanks also the Canada Foundation for Innovation, the Ontario Innovation Trust, the Canada Research Chair Secretariat and the Province of Ontario for a Premier's Research Excellence Award. We thank Ian Swainson of the Neutron Program for Materials Research, NRC of Canada, for assistance with the collection of neutron diffraction data at the Chalk River Nuclear Laboratories, J.D. Garrett for assistance with sample preparation and J.F. Britten for assistance with the single crystal data collection and analysis.

References

[1] C.A. Bridges, J.E. Greedan, J. Solid State Chem. 177 (2004) 1098.
[2] O.K. Andersen, Phys.Rev. B 12 (1975) 3060.
[3] G. Liu, J.E. Greedan, J. Solid State Chem. 122 (1996) 416.
[4] S.A. Shivashankar, J.M. Honig, Phys. Rev. B 28 (1983) 5695.
[5] F.J. Morin, Phys. Rev. Lett. 3 (1959) 34.
[6] J. Akimoto, Y. Gotoh, M. Sohma, K. Kawaguchi, Y. Oosawa, J. Solid State Chem. 113 (1994) 384.
[7] Y. Kanke, F. Izumi, E. Takayama-Muromachi, K. Kato, J. Solid State Chem. 92 (1991) 261.
[8] H.L. Skriver, The LMTO Method, Springer, Berlin, Germany, 1984.
[9] L. Hedin, B.I. Lundquist, J. Phys. 4C (1971) 2064.
[10] P. Blöchl, O. Jepsen, O.K. Andersen, Phys. Rev B 49 (1994) 16223.
[11] G.M. Sheldrick, SHELXL97, Program for the Refinement of Crystal Structures, Univ. of Gottingen, Germany, 1997.
[12] G.M. Sheldrick, SADABS, Siemens Area Detector Absorption Correction Software, Univ. of Göttingen, Germany, 1997.
[13] G. Amow, N.P. Raju, J.E. Greedan, J. Solid State Chem. 155 (2000) 177.
[14] R. Dronskowski, P.E. Blöchl, J. Phys. Chem. 97 (1993) 8617.
[15] G.A. Landrum, R. Dronskowski, Angew. Chemie Intl. Ed. 39 (2000) 1560.
[16] S. Derakhshan, A. Assoud, K.M. Kleinke, E. Dashjav, X. Qiu, S.J.L. Billinge, H. Kleinke, J. Am. Chem. Soc. 126 (2004) 8295.
[17] N.F. Mott, Conduction in Non-Crystalline Materials, Oxford Press, Oxford, 1987, p. 20ff.
[18] R.D. Shannon, Acta. Crystallogr. A 32 (1976) 751.
[19] I.D. Brown, D. Altermatt, Acta. Cryst. B 41 (1985) 244; A.S. Wills, VaList for GSAS, 1998.
[20] P. Schiffer, A.P. Ramirez, Comm. Condens. Matter Phys. 10 (1996) 21.
[21] Y. Ueda, K. Kosuge, S. Kachi, J. Solid State Chem. 31 (1980) 171.
[22] N.F. Mott, E.A. Davis, Electronic Processes in Non-Crystalline Materials, Clarendon Press, Oxford, 1971, p. 42.
[23] A.L. Efros, B.I. Shklovskii, J. Phys. C: Solid State Phys 8 (1975) L49.
[24] R.M. Hill, Phys. Stat. Solidi A 35 (1976) K29; A.G. Zabrodski, Sov. Phys. Semicond. 11 (1977) 345.
[25] P.M. Chaikin, in: V.Z. Kresin, W.A. Little (Ed.), An introduction to thermopower for those who might want to use it to study organic conductors and superconductors. Organic Superconductors, Interscience Publishers, New York, 1990, pp. 101–115.
[26] P.W. Anderson, Phys. Rev. 109 (1958) 1492.